metals

MDPI

Article

Surface Morphologies and Mechanical Properties of Mg-Zn-Ca Amorphous Alloys under Chemistry-Mechanics Interactive Environments

Yongyan Li [1,2,†], Zhuofan Liang [1,†], Lianzan Yang [1,†], Weimin Zhao [1,*], Yalong Wang [1,*], Hui Yu [1], Chunling Qin [1] and Zhifeng Wang [1,2,*]

1 School of Materials Science and Engineering, Hebei University of Technology, Tianjin 300130, China; liyongyan@126.com (Y.L.); zfliang2017mail@163.com (Z.L.); yanglianzan@163.com (L.Y.); yuhuidavid@126.com (H.Y.); clqin@hebut.edu.cn (C.Q.)

2 Key Laboratory for New Type of Functional Materials in Hebei Province, Hebei University of Technology, Tianjin 300130, China

* Correspondence: wmzhao@yahoo.com (W.Z.); yalongwang97@163.com (Y.W.); zfwangmail@163.com (Z.W.); Tel.: +86-22-60204477 (W.Z.); +86-187-2236-5301 (Y.W.); +86-22-60204129 (Z.W.)

† These authors contributed equally to this work.

Received: 24 February 2019; Accepted: 13 March 2019; Published: 14 March 2019

Abstract: Mg-Zn-Ca amorphous alloys are considered as potential bone implants. A large number of works have focused on the alloys under free corrosion environment. However, the real service environment of bone implants is a kind of chemistry-mechanics interactive environment in which the materials not only suffer corrosion by body fluids but also bear applied force induced by body movement. In order to imitate the real service environment, surface morphologies and mechanical properties of Mg-Zn-Ca amorphous alloys were studied under different chemistry-mechanics interactive environments in this paper. It was found that cracks and Ca/Mg phosphates formed on the surface of amorphous alloys. The compressive strength of the alloys decreased seriously but could still reach an acceptable value to avoid material failure. Fan-shaped patterns found on all the samples implied that brittle fracture was the main fracture form. Moreover, vein-like patterns could still be found in some areas, showing a locally plastic deformation. This was the reason why the alloy could maintain a high compressive strength after severe and interactive treatments. The study could guide related works in the establishment of experimental environments in the future, which will facilitate a more accurate biomedical evaluation of bone implants.

Keywords: Mg-Zn-Ca; amorphous alloy; mechanical property; interactive environment

1. Introduction

Magnesium (Mg) alloys are regarded as potential orthopedic implants and bone repairing materials due to low density, proper elasticity, high strength-to-weight ratio, good biodegradability, and bioabsorbability [1–3]. This study focused on the popular Mg-Zn-Ca biomaterials [4,5] containing safe and non-toxic component elements. Compared to traditional crystalline Mg-Zn-Ca alloys, Mg-Zn-Ca amorphous alloys exhibit a higher compressive strength and corrosion resistance for their uniform composition distribution and almost no crystal defects [4,6]. Thus, the study of mechanical and corrosion properties of Mg-Zn-Ca amorphous alloys is very meaningful.

Recently, great attention has been paid by global researchers to the study of Mg-Zn-Ca-based amorphous alloys in different research point of views. Zheng et al. [7] carried out cytotoxicity tests on Mg-Zn-Ca amorphous alloys. The amorphous alloy showed better cytoactivity than the rolled pure Mg. Löffler et al. [8] restrained hydrogen evolution during animal implantation

experiments, which promoted the exploitation of Mg-Zn-Ca amorphous alloys in biomedical applications. Durandurdu et al. [9] revealed atomic structures and mechanical properties of Mg-Zn-Ca amorphous alloys through the first principle method. Guo et al. [10] improved the mechanical and corrosion properties of Mg-Zn-Ca amorphous alloys by the introduction of porous NiTi shaped memory alloy particles. Moreover, the effects of element ratio and cooling rate [11–13], as well as the effects of Mn, Sr, Ti, Si, Ag, Y, Yb, Nd, Cu, Fe, and Pd additives [14–26] on microstructure, mechanical properties, and corrosion resistance of Mg-Zn-Ca amorphous alloys were studied in detail.

It is worth noting that a free corrosion environment was adopted in nearly all the previous works. However, some experimental design defects existed in the reported studies. In fact, the real service environment of bone implant materials is a kind of chemistry-mechanics interactive environment in which the materials not only suffer corrosion by body fluids but also bear applied force induced by body movement. In order to imitate the real service environment of implant materials, the surface morphologies and mechanical properties of Mg-Zn-Ca amorphous alloys were studied under different chemistry-mechanics interactive environments in this paper. The work would be a useful supplement to the previous studies. In addition, relevant experimental conditions could guide the future works in this field, which will facilitate a more accurate biomedical evaluation of bone implant materials.

2. Materials and Methods

2.1. Materials Preparation

$Mg_{62.9}Zn_{32.3}Ca_{4.8}$ (at.%) amorphous alloys were fabricated by a process similar to that stated in our previous work [14]. Firstly, $Mg_{62.9}Zn_{32.3}Ca_{4.8}$ ingots were melted by high purity Mg ingot (99.99 wt.%), Zn ingot (99.99 wt.%), and Mg-30.5 wt.% Ca master alloys at 760 °C in a crucible electric resistance furnace (SG_2-5-10A) under CO_2/SF_6 mixed atmosphere. Secondly, the master alloys were remelted twice to obtain a homogenous microstructure. Thirdly, the ingots were remelted by induction melting and subsequently produced into metal rods (φ2 mm × 4 cm) by copper mold spray casting method. Finally, the amorphous samples were machined into the size of φ2 mm × 4 mm for further tests.

2.2. Chemistry-Mechanics Interactive Experiments

The experimental facility offering a chemistry-mechanics interactive environment is shown in Figure 1. The samples were immersed in simulated body fluid (SBF) at 37 ± 1 °C and pressed by different pressures at the same time. The chemical composition of the SBF solution (g/L) [27] was 8.0 NaCl, 0.4 KCl, 1.0 glucose, 0.09 $Na_2HPO_4 \cdot 7H_2O$, 0.19 $CaCl_2 \cdot 2H_2O$, 0.2 $MgSO_4 \cdot 7H_2O$, 0.35 $NaHCO_3$, and 0.06 KH_2PO_4. The detailed treatment conditions to experimental alloys and the sample numbers are listed in Table 1. Particularly, different chemistry-mechanics interactive environments including free corrosion, constant pressure corrosion, intermittent pressure corrosion, and variable pressure corrosion were performed in this study.

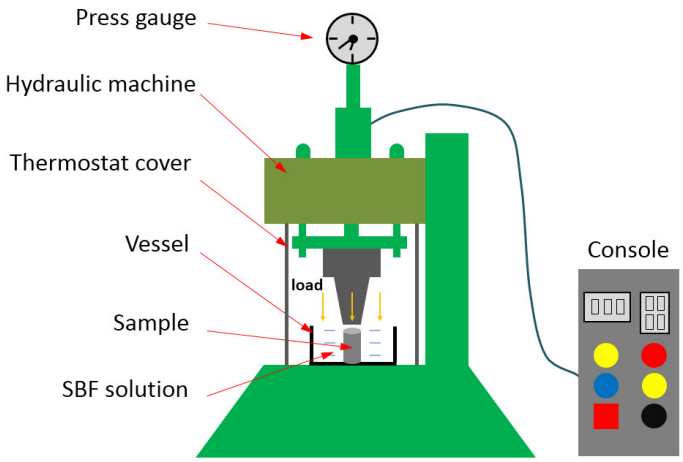

Figure 1. Schematic of the experimental facility that offers a chemistry-mechanics interactive environment.

Table 1. Different treatment conditions of experimental alloys.

Sample Number	Treatment Condition		
	Load	**Corrosion Time**	**Notes**
Sample 1	150 MPa	1 h	Constant pressure corrosion
Sample 2	150 MPa	3 h	
Sample 3	150 MPa	5 h	
Sample 4	30 MPa	3 h	
Sample 5	90 MPa	5 h	
Sample 6	0 MPa	5 h	Free corrosion
Sample 7	0 MPa/0.5 h + 150 MPa/0.5 h + 0 MPa/0.5 h + 150 MPa/0.5 h Total: 5 h		Intermittent pressure corrosion
Sample 8	30 MPa/0.5 h + 90 MPa/0.5 h + 150 MPa/0.5 h + 30 MPa/0.5h + 90 MPa/0.5 h + 150 MPa/0.5 h Total: 5 h		Variable pressure corrosion

2.3. Microstructure and Mechanical Properties

The phase structure of the original sample was measured through XRD (D8, Bruker, Karlsruhe, Germany) with a Cu K_α radiation. The surface morphologies of the samples before and after corrosion as well as fracture morphologies after compression tests were analyzed using SEM (JSM-IT300, JEOL, Tokyo, Japan) equipped with energy-dispersive spectroscopy (EDS). The surface characteristic of the amorphous alloy after variable pressure corrosion was measured by FTIR (Vertex 80V, Bruker, Karlsruhe, Germany). The compressive tests were conducted with an UTM5105X testing machine at room temperature.

3. Results and Discussion

Figure 2a shows the surface SEM image of the original copper mold spray casted $Mg_{62.9}Zn_{32.3}Ca_{4.8}$ alloys, indicating a uniform microstructure with no precipitated phase. Figure 2b shows the XRD result of the sample. It presents typical broad (diffuse-scattering) peaks. Both the SEM image and the XRD data demonstrate that the as-obtained Mg-Zn-Ca alloy was indeed an amorphous alloy.

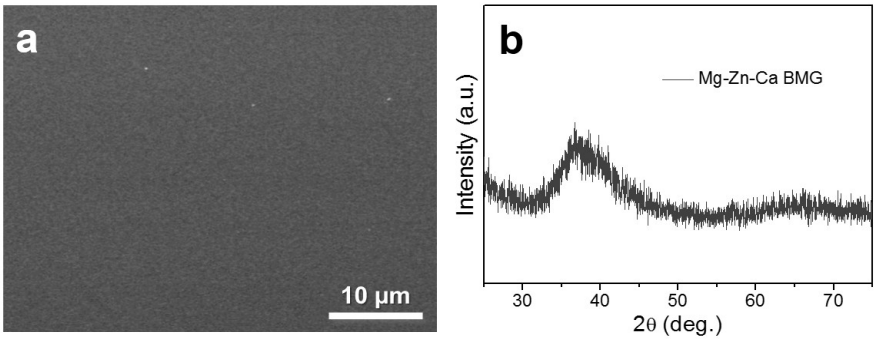

Figure 2. SEM image (**a**) and XRD patterns (**b**) of the original copper mold spray casted $Mg_{62.9}Zn_{32.3}Ca_{4.8}$ alloy.

Figure 3a–e shows SEM images of surface morphologies of Mg-Zn-Ca amorphous alloys after constant pressure corrosion. Thereinto, Figure 3a–c reveals the surface morphologies of Samples 1–3 under 150 MPa constant pressure corrosion conditions. It can be seen from Figure 3a that when the corrosion time was 1 h, the sample was not seriously corroded or deformed. Some cracks and pits began to form, and a small amount of particles covered the surface. When the corrosion time expanded to 3 h (Figure 3b), obvious cracks and many Ca/Mg phosphate particles were generated on the sample surface. Parts of the particles gathered together to become Ca/Mg phosphate layers. After 5 h of corrosion (Figure 3c), the cracks deepened. The primary and secondary cracks continued to expand forward. At the same time, Ca/Mg phosphate layers with certain thickness covered almost the entire surface of the sample. The layer crazed under the impact of external force. SEM images of surface morphologies of Mg-Zn-Ca amorphous alloys after 3 h of corrosion with different pressures are shown in Figure 3d,e, and b. When the pressure was set at 30 MPa (Figure 3d), a small number of micro-cracks accompanied by a certain number of $Mg(OH)_2$ microwires [28,29] formed on the sample surface. When the pressure was increased to 90 MPa (Figure 3e), the crack grew and spread. $Mg(OH)_2$ microwires could also be found in this situation. A magnified image revealed that the microwire presented a screw thread shape with a diameter of 300~400 nm. When the pressure was further increased to 150 MPa (Figure 3b), a large number of secondary cracks appeared beside the primary crack. In the meantime, Ca/Mg phosphates in the form of particle clusters were generated on the sample surfaces. Figure 3f displays the EDS results of areas A, B, and C in Figure 3a–c, respectively. It was found that the three areas mainly contained five elements including Mg, Zn, Ca, O, and P. With the extension of corrosion time, the proportion of O and P increased gradually, indicating the content of Ca/Mg phosphates enhanced. This result was in accord with the variation trend in surface coverage rate of Ca/Mg phosphates observed by SEM images. Calcium phosphates, regarded as potential precursors of hydroxyapatites, were found to be effective for bone induction. In addition, hydroxyapatite possesses good biocompatibility, bioactivity, and bone growth guidance effects, which is chemically and structurally similar to the inorganic components of bone. That suggests Mg-Zn-Ca amorphous alloys possess excellent biocompatibility under interactive environments when applied as orthopedic implants. The above analysis shows that when the corrosion time is prolonged (constant pressure) or the pressure is increased (constant time), the cracks increase, spread, and deepen gradually. Under a relatively small pressure, only $Mg(OH)_2$ microwires can be formed, while under a higher pressure, the nucleation and growth of Ca/Mg phosphates can be promoted. The relevant formation mechanism is worthy of investigation in future works.

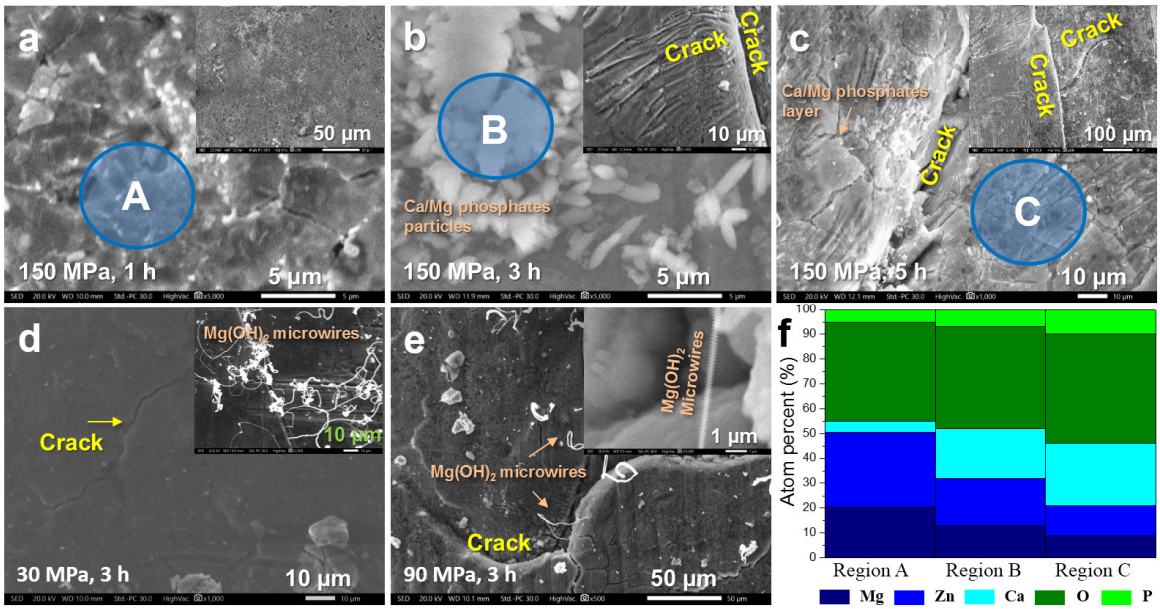

Figure 3. SEM images showing surface morphologies of Mg-Zn-Ca amorphous alloys after constant pressure corrosion: (**a**) Sample 1; (**b**) Sample 2; (**c**) Sample 3; (**d**) Sample 4; (**e**) Sample 5; (**f**) energy-dispersive spectroscopy (EDS) analysis of areas A, B, C in (**a**), (**b**), and (**c**), respectively.

Figure 4 shows surface SEM morphologies of Mg-Zn-Ca amorphous alloys after free corrosion, intermittent pressure corrosion, and variable pressure corrosion. After the free corrosion (Figure 4a,b), there were some pits and a few $Mg(OH)_2$ microwires on the sample surface without any cracks, demonstrating a low damage degree of the sample. After the intermittent pressure corrosion (Figure 4c,d), apparent cracks could be seen on the sample surface. A step was formed, as shown in Figure 4d, in this situation. Meanwhile, a certain amount of Ca/Mg phosphates particles were generated on the sample surfaces. After the variable pressure corrosion, deeper cracks and a mass of Ca/Mg phosphates microspheres formed. Thereout, the surface of the samples changed greatly under chemistry-mechanics interactive environments compared with free corrosion conditions. On the one hand, a large number of cracks appeared. On the other hand, Ca/Mg phosphates, as corrosion products, increased obviously. Moreover, compared to intermittent pressure corrosion, deeper cracks and more corrosion products could be obtained under variable pressure corrosion. This was because longer and continuous chemistry-mechanics interactive environments promoted the corrosion/degradation of surface metals and accelerated the formation of Ca/Mg phosphates. It could be speculated that both the cracks and the Ca/Mg phosphates were generated for bone implants when the body moved. This possible creation of cracks was not observed under the free corrosion conditions. Its perniciousness should be noted. Furthermore, the formation of Ca/Mg phosphates is favorable for generating hydroxyapatites, which may improve the biocompatibility, while the creation of cracks tends to decrease the service life of the implants. Thus, the balance of the two aspects is of great importance and needs detailed studying in future works.

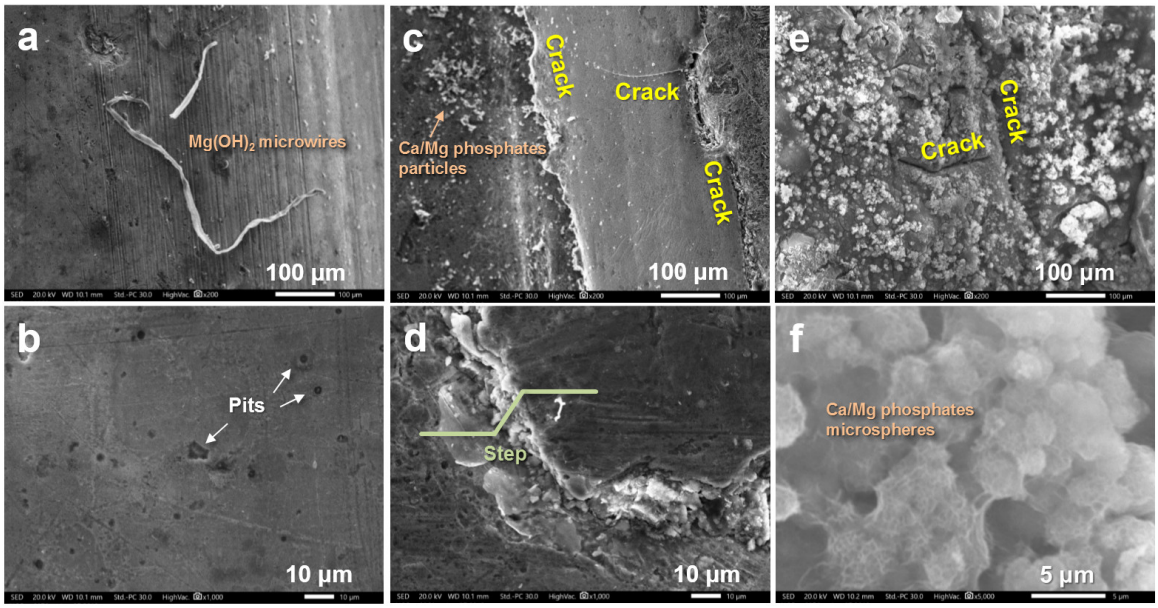

Figure 4. SEM images showing surface morphologies of Mg-Zn-Ca amorphous alloys after different interactive experiments: (**a**,**b**) free corrosion, Sample 6; (**c**,**d**) intermittent pressure corrosion, Sample 7; (**e**,**f**) variable pressure corrosion, Sample 8.

Figure 5a presents a highly magnified SEM image of Sample 8, showing a clear microstructure of microspheres. The EDS result shown in Figure 5b displays the composition of the microspheres, including Mg, O, Fe, Cl, P, and Ca. Thereinto, Cl and P came from the SBF solution, while Fe was from the experimental container in which the materials were placed. The Ca/P atom ratio was approximately equal to 1.0, demonstrating that calcium phosphates were possibly generated. Moreover, the previously disregarded introduction of Fe greatly affected the morphology of calcium phosphates. Such a phenomenon was also reported in a previous work [30]. These results provided a new idea for the morphological control of calcium phosphates in the future. It was found that the spherical structure with large surface area was an ideal structure for bone adhesives. When the spherical bone adhesives were evenly distributed, the migration of bone cells and the growth of extracellular matrix could be promoted by the vacancy among spherical particles. Therefore, the controlled synthesis of spherical calcium phosphates on the surface of Mg alloys is worthy of study in the future. Figure 5c reflects FTIR results of Sample 8. The absorption peaks of the spectra located at 570 and 1010 cm^{-1} could be assigned to the phosphate group [14], which was created from the following reactions [31,32] and further confirmed the formation of Ca/Mg phosphates.

$$Mg + 2H_2O \rightarrow Mg^{2+} + 2OH^- + H_2 \quad (1)$$

$$Mg^{2+}\ (\text{or } Ca^{2+}) + OH^- + HPO_4{}^{2-} + (n-1)\,H_2O \rightarrow Mg(\text{or } Ca)_x \cdot (PO_4)_y \cdot nH_2O \quad (2)$$

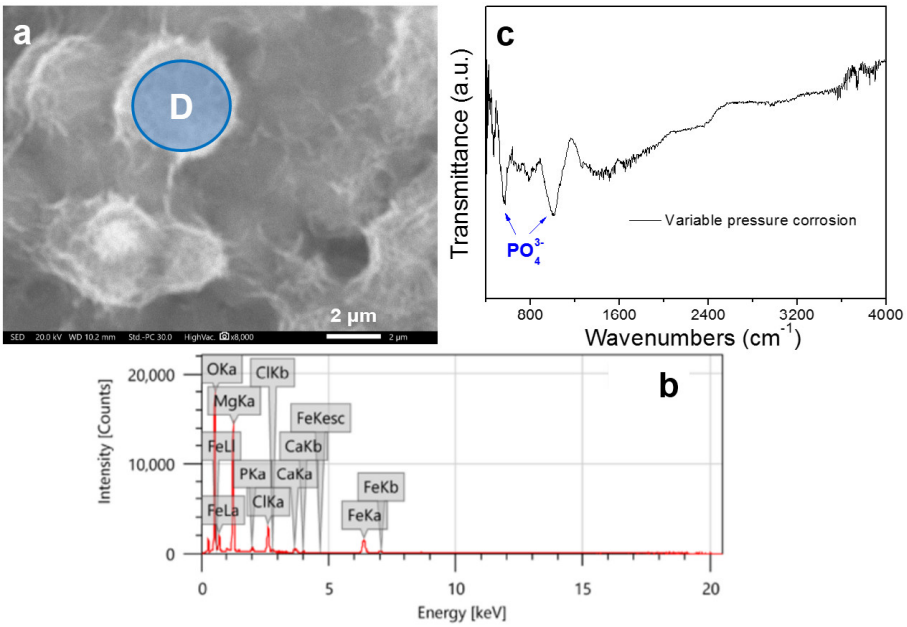

Figure 5. (**a**) Highly magnified SEM image of Sample 8; (**b**) EDS analysis of area D in (**a**); (**c**) superficial FTIR analysis of Sample 8.

Figure 6 shows the mechanical properties of the experimental samples. It can be seen in Figure 6a that the compressive strength of the original Mg-Zn-Ca amorphous alloy was 589.8 MPa. Figure 6b–d presents the compression test curves of amorphous alloys under different chemistry-mechanics interactive environments. When the constant pressure was set at 150 MPa (Figure 6b), the compressive strength decreased from 436.1 MPa to 106.6 MPa with the corrosion time increased from 1 h to 5 h. According to the analysis from Figure 6e, the data conformed to the linear rule. That is to say, under a certain pressure, the compressive strength decreased linearly with the increase of corrosion time in the interactive experiment. It can be further predicted that when the corrosion time is extended to about 6.2 h, the amorphous alloy will be broken and the compressive strength will approach zero. When the corrosion time was set at 3 h (Figure 6c), the compressive strength decreased from 513.9 MPa to 305.4 MPa with the pressure increased from 30 MPa to 150 MPa. Polynomial fitting was performed on the data. It can be seen from Figure 6f that the compressive strength reduced gradually with the increasing pressure. It can also be predicted that when the pressure is enhanced to about 260 MPa, the amorphous alloy will be broken and the compressive strength will tend toward zero. Figure 6d presents the compression test curves of amorphous alloys under free corrosion, intermittent pressure corrosion, and variable pressure corrosion conditions for 5 h. It can be seen that the compressive strength of the sample after free corrosion was the highest, which reached 428.1 MPa. The sample corroded under variable pressure had the lowest compressive strength (349.4 MPa). It was found that the compressive strength of the amorphous alloys decreased seriously in the interactive experiment but could still reach an acceptable value to avoid material failure. The value approximately equaled the highest compressive strength of conventional extruded Mg alloys, showing a great superiority of amorphous alloys in compressive strength compared to crystalline Mg alloys under corrosion environments.

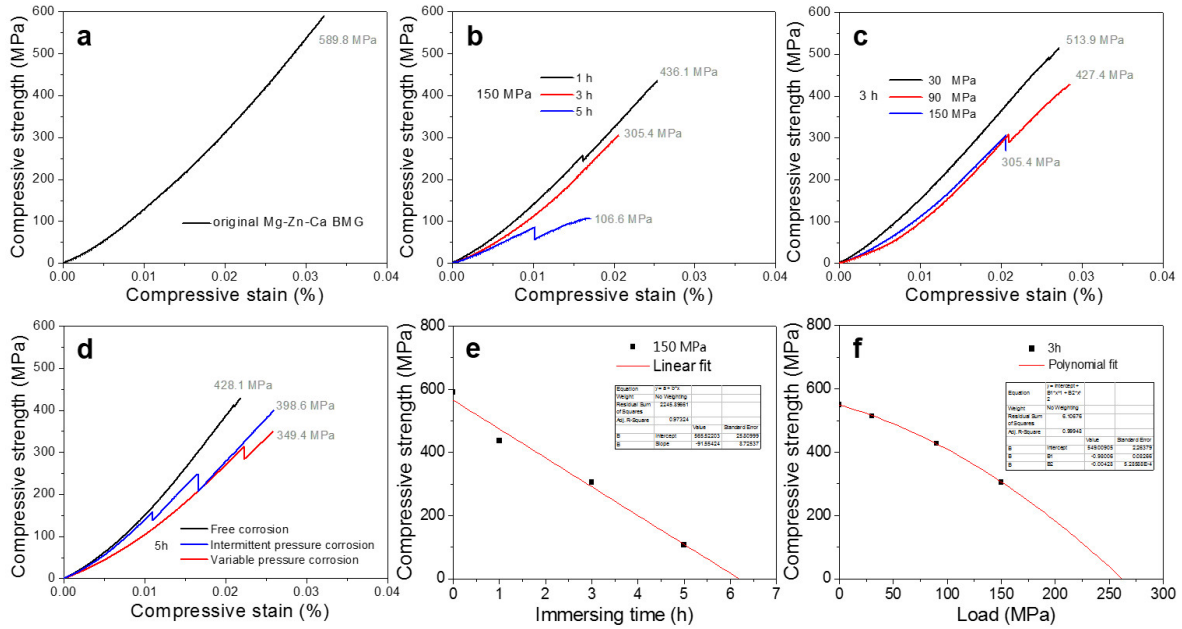

Figure 6. Compressive curves of original Mg-Zn-Ca amorphous alloys (**a**), Sample 1–3 (**b**), Sample 2, 4 and 5 (**c**); (**d**) Sample 6–8; (**e**) linear fitting of (**b**); (**f**) polynomial fitting of (**c**).

Figures 7 and 8 present fracture morphologies of experimental amorphous alloys after different treatments. Figure 7a reflects the fracture morphology of the original Mg-Zn-Ca amorphous alloy. A mass of herringbone patterns and local vein-like patterns could easily be found, which illustrated that brittle fracture was the main fracture form in the original alloy, accompanied by local plastic deformation. The fracture morphologies of amorphous alloys after different constant pressure corrosion are shown in Figure 7b–f. Although the amorphous alloys were treated under different pressures matched with diverse corrosion time, fan-shaped patterns, clear cracks, and shear bands could be seen on all the fractures. These results showed that brittle fracture was the main fracture form for the samples treated with constant pressure corrosion. Figure 8 shows fracture morphologies of amorphous alloys after free corrosion, intermittent pressure corrosion, and variable pressure corrosion. Obvious fan-shaped patterns, cracks, and shear bands could also be found easily. It can be seen that the fracture patterns of the samples did not change significantly by free corrosion or by interactive environment corrosion. It should be noted that although 5 h of variable pressure corrosion treatment was carried out, a vein-like pattern could still be found in local areas of Sample 8, indicating that the alloy still contained plastic deformation locally. This was the reason why the alloy could maintain more than 300 MPa of compressive strength after being subjected to variable pressure corrosion.

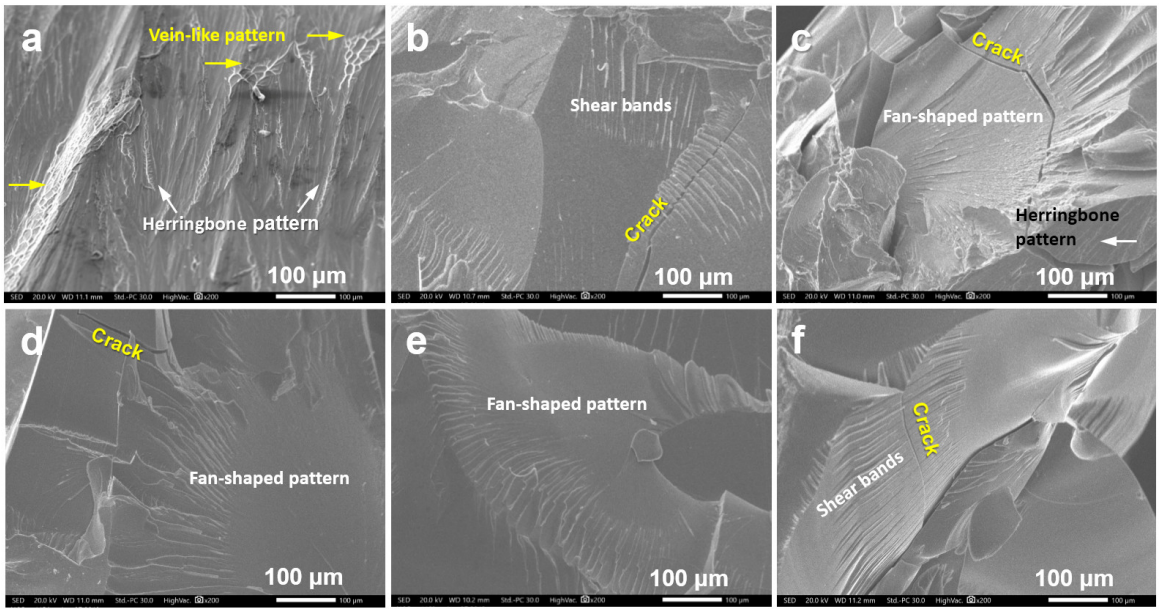

Figure 7. SEM images of fracture morphologies of the experimental alloys: (**a**) original Mg-Zn-Ca amorphous alloy; (**b**) Sample 1; (**c**) Sample 2; (**d**) Sample 3; (**e**) Sample 4; (**f**) Sample 5.

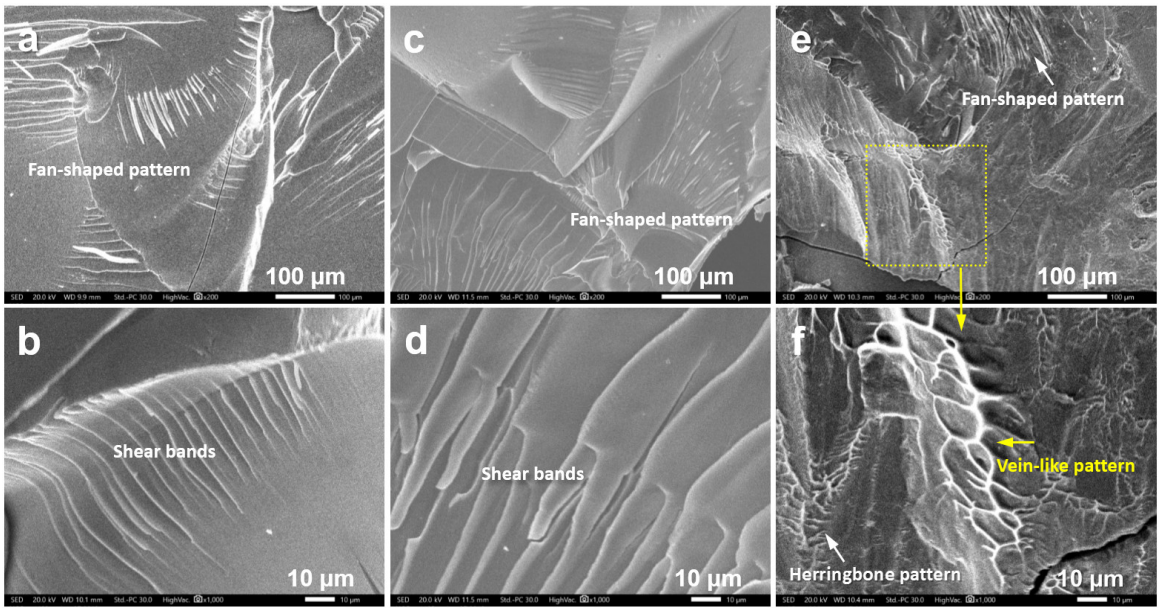

Figure 8. SEM images of fracture morphologies of the experimental alloys: (**a**,**b**) Sample 6; (**c**,**d**) Sample 7; (**e**,**f**) Sample 8.

In this paper, we designed and performed experiments under different chemistry-mechanics interactive environments to imitate the real situation of bone implants. It should be noted that, although this is the first paper related to interactive experiments in this research field, there are some differences between interactive environments in this paper and in real service environments, which needs improving in future works. First, some extremely high pressure conditions were adopted in the paper to speed up the experimental process; a more reasonable setting and adjustment on the interactive environments should be performed in the future. Second, the paper provided uniaxial compression onto samples, but the sample in real service environment suffered stress coming from different directions, including pressure, tension, and even torsion, thus the construction of a more complex service environment must be carried out in the future. Third, the work was carried out in

simulated body fluids—not in real animals—which may have caused different reactions and product morphologies. In conclusion, the interactive experiments under more real service environments need to be designed and studied in further detail. A lot of related works are worthy of being carried out in the future.

4. Conclusions

Surface morphologies and mechanical properties of Mg-Zn-Ca amorphous alloys under different chemistry-mechanics interactive environments were studied in this paper. It was found that cracks and Ca/Mg phosphates formed on the surface of amorphous alloys under different interactive environments. With the increase in corrosion time (constant pressure) or pressure (constant time), the cracks spread and deepened gradually. The compressive strength of the alloys decreased seriously in the interactive experiment but could still reach an acceptable value to avoid material failure. Fan-shaped patterns could be found on all the samples, indicating that brittle fracture was the main fracture form. Moreover, vein-like patterns could still be found in some areas, showing a locally plastic deformation. This was the reason why the alloy could maintain a high compressive strength after severe and interactive treatments. We showed the first paper performing an interactive experiment on potential bone implant materials. It is of referential significance in the design of related experiments. In addition, the interactive experiments under more real service environments need to be designed and studied in further detail in future works.

Author Contributions: Data curation, Y.L. and Z.L.; Formal analysis, L.Y., H.Y. and C.Q.; Funding acquisition, Z.W.; Investigation, Y.L., Z.L., L.Y. and Y.W.; Methodology, W.Z., Y.W. and Z.W.; Project administration, Z.W.; Resources, W.Z. and C.Q.; Supervision, W.Z., H.Y. and C.Q.; Writing—original draft, Y.L. and Z.L.; Writing—review & editing, Z.W.

Funding: This work is financially supported by Natural Science Foundation of Hebei Province, China (E2015202081) and Innovation & Entrepreneurship Training Program of Hebei University of Technology (201810080071).

Conflicts of Interest: The authors declare no conflict of interest.

References

1. Xiong, H.Q.; Liang, Z.F.; Wang, Z.F.; Qin, C.L.; Zhao, W.M.; Yu, H. Mechanical properties and degradation behavior of $Mg_{(100-7x)}Zn_{6x}Y_x$(x = 0.2, 0.4, 0.6, 0.8) alloys. *Metals* **2018**, *8*, 261. [CrossRef]
2. Wang, Z.F.; Zhao, W.M.; Li, H.P.; Ding, J.; Li, Y.Y.; Liang, C.Y. Effect of titanium, antimony, cerium and carbon nanotubes on the morphology and microhardness of Mg-based icosahedral quasicrystal phase. *J. Mater. Sci. Technol.* **2010**, *26*, 27–32. [CrossRef]
3. Wang, Z.F.; Zhao, W.M.; Hur, B.Y.; Huang, C.Y.; Yu, C.Q. Effects of the fourth component and undercooling on morphology of primary Mg-Zn-Y icosahedral quasicrystal phase under normal casting conditions. *China Foundry* **2009**, *6*, 293–299.
4. Yu, H.J.; Wang, J.Q.; Shi, X.T.; Louzguine-Luzgin, D.V.; Wu, H.K.; Perepezko, J.H. Ductile biodegradable Mg-based metallic glasses with excellent biocompatibility. *Adv. Funct. Mater.* **2013**, *23*, 4793–4800. [CrossRef]
5. Roche, V.; Koga, G.Y.; Matias, T.B.; Kiminami, C.S.; Bolfarini, C.; Botta, W.J.; Nogueira, R.P.; Jorge Junior, A.M. Degradation of biodegradable implants: The influence of microstructure and composition of Mg-Zn-Ca alloys. *J. Alloys Compd.* **2019**, *774*, 168–181. [CrossRef]
6. Wang, Z.F.; Liu, J.Y.; Qin, Q.L.; Yu, H.; Xia, X.C.; Wang, C.Y.; Zhang, Y.S.; Hu, Q.F.; Zhao, W.M. Dealloying of Cu-based metallic glasses in acidic solutions: Products and energy storage applications. *Nanomaterials* **2015**, *5*, 697–721. [CrossRef]
7. Gu, X.N.; Zheng, Y.F.; Zhong, S.P.; Xi, T.F.; Wang, J.Q.; Wang, W.H. Corrosion of, and cellular responses to Mg-Zn-Ca bulk metallic glasses. *Biomaterials* **2010**, *31*, 1093–1103. [CrossRef]
8. Zberg, B.; Uggowitzer, P.; Löffler, J.F. MgZnCa glasses without clinically observable hydrogen evolution for biodegradable implants. *Nat. Mater.* **2009**, *8*, 887–891. [CrossRef]
9. Erkartal, M.; Durandurdu, M. An in-depth investigation of Mg-Zn-Ca metallic glasses: A first principles study. *Comput. Mater. Sci.* **2018**, *153*, 326–337. [CrossRef]

10. Guo, W.; Kato, H.; Lü, S.L.; Wu, S.S. Porous NiTi particle dispersed Mg-Zn-Ca bulk metallic glass matrix composites. *Materials* **2018**, *11*, 1959. [CrossRef]
11. Nowosielski, R.; Cesarz-Andraczke, K. Impact of Zn and Ca on dissolution rate, mechanical properties and GFA of resorbable Mg–Zn–Ca metallic glasses. *Arch. Civ. Mech. Eng.* **2018**, *18*, 1–11. [CrossRef]
12. Matias, T.B.; Roche, V.; Nogueira, R.P.; Asato, G.H.; Kiminami, C.S.; Bolfarini, C.; Botta, W.J.; Jorge, A.M., Jr. Mg-Zn-Ca amorphous alloys for application as temporary implant: Effect of Zn content on the mechanical and corrosion properties. *Mater. Des.* **2016**, *110*, 188–195. [CrossRef]
13. Wang, J.F.; Huang, S.; Guo, S.F.; Wei, Y.Y.; Pan, F.S. Effects of cooling rate on microstructure, mechanical and corrosion properties of Mg−Zn−Ca alloy. *Trans. Nonferrous Met. Soc. China* **2013**, *23*, 1930–1935. [CrossRef]
14. Liang, Z.F.; Yang, L.Z.; Li, Y.Y.; Wang, X.; Qin, C.L.; Zhao, W.M.; Yu, H.; Wang, Z.F. Effects of Ag, Nd, and Yb on the microstructures and mechanical properties of Mg-Zn-Ca metallic glasses. *Metals* **2018**, *8*, 856. [CrossRef]
15. Wang, J.F.; Ma, Y.; Guo, S.F.; Jiang, W.Y.; Liu, Q.S. Effect of Sr on the microstructure and biodegradable behavior of Mg–Zn–Ca–Mn alloys for implant application. *Mater. Des.* **2018**, *153*, 308–316. [CrossRef]
16. Wang, J.L.; Wan, Y.; Ma, Z.J.; Guo, Y.C.; Yang, Y.; Wang, P.; Li, J.P. Glass-forming ability and corrosion performance of Mn-doped Mg–Zn–Ca amorphous alloys for biomedical applications. *Rare Met.* **2018**, *37*, 579. [CrossRef]
17. Chen, S.S.; Tu, J.X.; Hu, Q.; Xiong, X.B.; Wu, J.J.; Zou, J.Z.; Zeng, X.R. Corrosion resistance and in vitro bioactivity of Si-containing coating prepared on a biodegradable Mg-Zn-Ca bulk metallic glass by micro-arc oxidation. *J. Non-Cryst. Solids* **2017**, *456*, 125–131. [CrossRef]
18. Li, H.F.; Pang, S.J.; Liu, Y.; Liaw, P.K.; Zhang, T. In vitro investigation of Mg–Zn–Ca–Ag bulk metallic glasses for biomedical applications. *J. Non-Cryst. Solids* **2015**, *427*, 134–138. [CrossRef]
19. Qin, F.X.; Xie, G.Q.; Dan, Z.; Zhu, S.L.; Seki, I. Corrosion behavior and mechanical properties of Mg-Zn-Ca amorphous alloys. *Intermetallics* **2013**, *42*, 9–13. [CrossRef]
20. Li, H.F.; Pang, S.J.; Liu, Y.; Sun, L.L.; Liaw, P.K.; Zhang, T. Biodegradable Mg–Zn–Ca–Sr bulk metallic glasses with enhanced corrosion performance for biomedical applications. *Mater. Des.* **2015**, *67*, 9–19. [CrossRef]
21. Wang, J.F.; Li, Y.; Huang, S.; Wei, Y.Y.; Xi, X.F.; Cai, K.Y.; Pan, F.S. Effects of Y on the microstructure, mechanical and bio-corrosion properties of Mg-Zn-Ca bulk metallic glass. *J. Mater. Sci. Technol.* **2014**, *30*, 1255–1261. [CrossRef]
22. Qin, C.L.; Xiao, T.N.; Li, Y.Y.; Wang, Z.F.; Liu, L.; Xiong, H.Q.; Zhao, W.M. Corrosion behavior of Mg-Zn-Ca amorphous alloys with Nd addition in simulated body fluids. *China Foundry* **2014**, *11*, 503–509.
23. Zhao, Y.F.; Zhu, J.; Chang, L.; Song, J.G.; Chen, X.H.; Hui, X.D. Influence of Cu content on the mechanical properties and corrosion resistance of Mg−Zn−Ca bulk metallic glasses. *Int. J. Min. Met. Mater.* **2014**, *21*, 487–493. [CrossRef]
24. Wang, J.F.; Huang, S.; Li, Y.; Wei, Y.Y.; Xi, X.F.; Cai, K.Y. Microstructure, mechanical and bio-corrosion properties of Mn–doped Mg–Zn–Ca bulk metallic glass composites. *Mater. Sci. Eng. C* **2013**, *33*, 3832–3838. [CrossRef]
25. Wang, J.F.; Huang, S.; Wei, Y.Y.; Guo, S.F.; Pan, F.S. Enhanced mechanical properties and corrosion resistance of a Mg–Zn–Ca bulk metallic glass composite by Fe particle addition. *Mater. Lett.* **2013**, *91*, 311–314. [CrossRef]
26. González, S.; Pellicer, E.; Fornell, J.; Blanquer, A.; Barrios, L.; Ibáñez, E.; Solsona, P.; Suriñach, S.; Baró, M.D.; Nogués, C.; Sort, J. Improved mechanical performance and delayed corrosion phenomena in biodegradable Mg–Zn–Ca alloys through Pd-alloying. *J. Mech. Behav. Biomed.* **2012**, *6*, 53–62. [CrossRef]
27. Qin, C.L.; Hu, Q.F.; Li, Y.Y.; Wang, Z.F.; Zhao, W.M.; Louzguine-Luzgin, D.V.; Inoue, A. Novel bioactive Fe-based metallic glasses with excellent apatite-forming ability. *Mater. Sci. Eng. C* **2016**, *69*, 513–521. [CrossRef]
28. Wang, L.M.; Wu, T.H.; Cao, D.X.; Yin, J.L.; Wang, G.L.; Zhang, M.L. Self-growth of micro- and nano-structured $Mg(OH)_2$ on electrochemically anodised Mg–Li alloy surface. *J. Exp. Nanosci.* **2015**, *10*, 56–65. [CrossRef]
29. Hahn, R.; Brunner, J.G.; Kunze, J.; Schmuki, P.; Virtanen, S. A novel approach for the formation of $Mg(OH)_2$/MgO nanowhiskers on magnesium: Rapid anodization in chloride containing solutions. *Electrochem. Commun.* **2008**, *10*, 288–292. [CrossRef]

30. Park, S.Y.; Perikamana, S.K.M.; Park, J.H.; Kim, S.W.; Shin, H.; Park, S.P.; Jung, H.S. Osteoinductive superparamagnetic Fe nanocrystal/calcium phosphate heterostructured microspheres. *Nanoscale* **2017**, *9*, 19145–19153. [CrossRef]
31. Song, G.L.; Atrens, A. Corrosion mechanisms of magnesium alloys. *Adv. Eng. Mater.* **1999**, *1*, 11–33. [CrossRef]
32. Xin, Y.C.; Hu, T.; Chu, P.K. Degradation behavior of pure magnesium in simulated body fluids with different concentrations of HCO_3^-. *Corros. Sci.* **2011**, *53*, 1522–1528. [CrossRef]